RESEARCH ARTICLE | JUNE 01 2020

Measurements of 2D poloidal plasma profiles and fluctuations in ECRH plasmas using the heavy ion beam probe system in the TJ-II stellarator

R. Sharma ; P. O. Khabanov; A. V. Melnikov; C. Hidalgo; A. Cappa ; A. Chmyga; L. G. Eliseev; T. Estrada ; N. K. Kharchev ; A. S. Kozachek; L. I. Krupnik; A. Malaquias ; B. van Milligen ; A. Molinero; J. L. de Pablos; I. Pastor; V. N. Zenin

Phys. Plasmas 27, 062502 (2020)
https://doi.org/10.1063/1.5142996

Physics of Plasmas ARTICLE scitation.org/journal/php

Measurements of 2D poloidal plasma profiles and fluctuations in ECRH plasmas using the heavy ion beam probe system in the TJ-II stellarator

Cite as: Phys. Plasmas **27**, 062502 (2020); doi: 10.1063/1.5142996
Submitted: 19 December 2019 · Accepted: 30 April 2020 ·
Published Online: 1 June 2020

R. Sharma,[1,a)] P. O. Khabanov,[2,3] A. V. Melnikov,[2,3,4] C. Hidalgo,[5] A. Cappa,[5] A. Chmyga,[6] L. G. Eliseev,[2] T. Estrada,[5] N. K. Kharchev,[2,7] A. S. Kozachek,[6] L. I. Krupnik,[6] A. Malaquias,[1] B. van Milligen,[5] A. Molinero,[5] J. L. de Pablos,[5] I. Pastor,[5] and V. N. Zenin[2]

AFFILIATIONS

[1]IPFN, Instituto Superior Técnico, Universidade de Lisboa, 1049-001 Lisboa, Portugal
[2]National Research Centre "Kurchatov Institute," 123182 Moscow, Russia
[3]Moscow Institute of Physics and Technology, 141700 Dolgoprudny, Russia
[4]National Research Nuclear University MEPhI, 115409 Moscow, Russia
[5]Fusion National Laboratory, CIEMAT, 28040 Madrid, Spain
[6]Institute of Plasma Physics, NSC KIPT, 61108 Kharkov, Ukraine
[7]Prokhorov General Physics Institute of the Russian Academy of Sciences, 117942 Moscow, Russia

[a)]**Author to whom correspondence should be addressed:** rsharma@ipfn.ist.utl.pt

ABSTRACT

2D poloidal contour plots of plasma potential, plasma density, and their fluctuations have been measured in low density plasmas sustained by Electron Cyclotron Resonance Heating using a heavy ion beam probe (HIBP) system in the TJ-II stellarator. A HIBP has been used in the new energy scanning mode to obtain the measurements for a 2D poloidal cross section of the stellarator. The 2D map for the absolute plasma potential shows a local maximum in the plasma core as expected in low density plasma scenarios. Fluctuations in the HIBP secondary ion current, as a proxy of plasma density fluctuations, appear both in positive and negative density gradient regions, with a normalized level of density fluctuations higher in the negative density gradient region. The TJ-II innovative experimental setup developed using a dual HIBP diagnostic paves the way for model validation on core plasma potential asymmetries and particle transport and fluctuations under positive and negative density gradient scenarios.

I. INTRODUCTION

Understanding and predicting particle and energy transport driven by turbulence is a key research issue in magnetically confined fusion plasmas. Upcoming fusion devices, like ITER, will explore plasma regimes that are far from present devices in many aspects. Therefore, extrapolations from purely empirical data can be misleading; thus, reliable data are required to validate models in existing plasma scenarios.

The characterization of plasma potential and its fluctuations is an important topic to understand and validate transport mechanisms in magnetically confined fusion plasmas.[1] The search for asymmetries in edge plasma fluctuations has shown the importance of curvature driven instabilities in the plasma boundary region.[2] First direct experimental evidence of strong poloidal Reynold stress asymmetry also points out the curvature driven zonal flow, which is similar to the asymmetry observed in turbulent transport.[3] In addition, flux-surface variations of electrostatic potential can have a significant impact on high-Z impurity radial fluxes.[4–6] Radial electric field asymmetries have been measured at the TJ-II stellarator that could be explained to be due to plasma potential variations within the flux surfaces.[7,8] Gyrokinetic (GK) simulations in stellarators show a strong localization of unstable modes along flux surfaces.[7,9,10] 2D core and edge density fluctuations have been previously investigated using beam emission spectroscopy[11] and fast visible cameras.[12] The first attempt to measure 2D spatial potential profiles has been done by a heavy ion beam probe in the large helical device (LHD) stellarator[13] covering less than $\frac{1}{4}$ of the poloidal plasma cross section.

Another important factor contributing to particle transport is density gradient localization, which is closely connected to the refueling of next step tokamaks and stellarator devices. Fueling of core

plasma particles is expected to be achieved with pellet systems that inject particles at high speed deep into the plasma. However, at reactor relevant plasma densities and temperatures, pellets are unable to reach the core plasma region. In fact, pellet ablation will take place in the plasma edge region[14–17] causing plasma bumps with positive and negative density gradient regions where eventually particles could be transported radially inwards by turbulence. Fluid and GK simulations have investigated the level of inward turbulent particle transport in the inverted density gradient region,[18–20] but comparisons of simulations with experimental fluctuation levels and fluxes are still missing. A TJ-II stellarator is well suited to investigate the influence of such positive and negative density gradients on plasma fluctuations and transport due to their unique capabilities to control plasma scenarios and magnetic configuration.[21]

The unique diagnostic set of dual heavy ion beam probes[22] (HIBPs) in TJ-II has shown the capabilities to simultaneously obtain the local mean and fluctuating measurements of plasma potential, plasma density, and poloidal magnetic field components with a spatial resolution of 1–2 cm and a sampling rate of 2 MHz. For the first time, the HIBP diagnostic has been operated in the energy scanning mode to investigate the 2D poloidal cross section of TJ-II as the injected primary beam energy is varied. This paper reports on the first attempt to experimentally characterize 2D poloidal structures of plasma profiles using the HIBP diagnostic in low density Electron Cyclotron Resonance Heated (ECRH) plasmas in the TJ-II stellarator. Compared to the recent study of ECRH effects on the plasma potential spatial profiles and turbulence,[23,24] the present work allows for the production of 2D contour maps of plasma potential and fluctuations from the high field side (HFS) to the low field side (LFS). In addition, the influence of plasma heating on plasma density fluctuations has been investigated. Both results provide the experimental basis for future model validation of core plasma potential asymmetries and plasma stability in positive and negative gradient regions.

II. EXPERIMENTAL SETUP

A TJ-II stellarator, with major radius $R = 1.5$ m and minor radius $a < 0.20$ m, has a unique experimental arrangement of a dual HIBP system.[25] In the experiments reported in this paper, both HIBP-I and HIBP-II systems were operated in scanning and fixed point mode from the high to the low field side (HFS to LFS) regions. The point of ionization or sample volume (SV) probed by the injecting beam inside the plasma in a poloidal cross section depends on the energy of the primary ion beam (Cs^+), determined by beam energy (E_b), and on the control voltages on the four sets of steering plates in the primary beam line to scan the beam from the HFS to LFS. Experiments for the 2D poloidal scans were carried out in pure Electron Cyclotron Resonance Heated (ECRH) regimes ($P_{ECRH} \approx 300$ kW at 53.2 GHz, second harmonic, X-mode polarization) with constant low density in the range $n_e \sim 0.4–0.5 \times 10^{19}$ m^{-3} and central electron temperature in the range $T_e \sim 1$ keV. Experiments were performed for the standard magnetic configuration of TJ-II with the edge rotational transform value close to 1.6 and a discharge duration of about 200 ms.

The experiment was organized as follows. At the first stage, the radial plasma profiles were obtained over the 1D detector line[1] with a probing beam energy of $E_b = 132$ keV, passing from the LFS through the plasma center to the HFS, by varying the injection angle into the plasma (control voltage). Then, the beam energy was changed in steps of 2 keV from 128 to 148 keV. With each step, the beam energy moves the detector line upwards by about 1 cm and forms a 2D detector grid. Hence, approximately 10×20 cm^2 of the plasma cross section was observed from the LFS to HFS for this experiment. Measurements of local mean and relative fluctuations in plasma density and potential were obtained using a parallel plate 30° energy analyzer in HIBP II. The multi-slit analyzer has five input slits that observes the five neighboring plasma SVs simultaneously to measure plasma parameters mentioned before.

Figure 1 shows the 2D detector grid probed by the Cs^+ primary beam in the poloidal cross section varying the beam energy in the range of 128–148 keV. The primary beam is radially scanned covering HFS and LFS regions in the TJ-II poloidal cross section. The time for each scan is fixed at 40 ms, so that we obtained four scans in the steady-state phase of discharge.

In addition, the experimental data for the investigation of the influence of ECRH scenarios on the plasma fluctuations are also presented. The discharges were carried out for the low density ($n_e \approx 0.4–0.6 \times 10^{19}$ m^{-3}) on-axis ($\rho \approx 0$) and off-axis ($\rho \approx 0.35$) ECRH scenarios. Figure 2 shows the temperature and density profiles for on-axis and off-axis discharges. The temperature profile for off-axis ECRH is flattened at the center as compared to the peaked profile at the center for on-axis ECRH. On-axis ECRH plasmas are characterized by peaked electron temperature and hollow density profiles as measured by Thomson Scattering (Fig. 2). The beam from HIBP-II was scanned from the HFS to LFS and power spectral densities for fluctuations were investigated.

III. EXPERIMENTAL RESULTS AND DISCUSSION

A 2D poloidal density and potential scans in ECRH on-axis experiments

The 2D analysis of averaged and the root mean square (RMS) of fluctuations for plasma potential and secondary ion current (I_{tot}) is

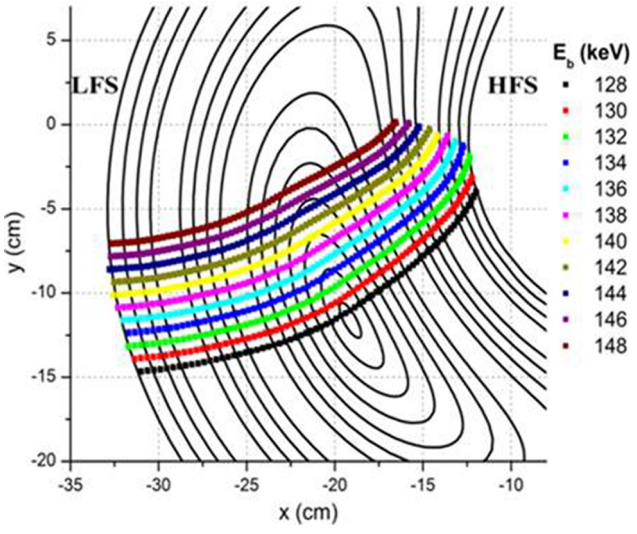

FIG. 1. HIBP detector grid for the vertical cross section of TJ-II for Cs^+ probing ions. The detector grid consists of 11 detector lines of equal energy E_b. Each detector line scans plasma vertical cross sections from the HFS to LFS.

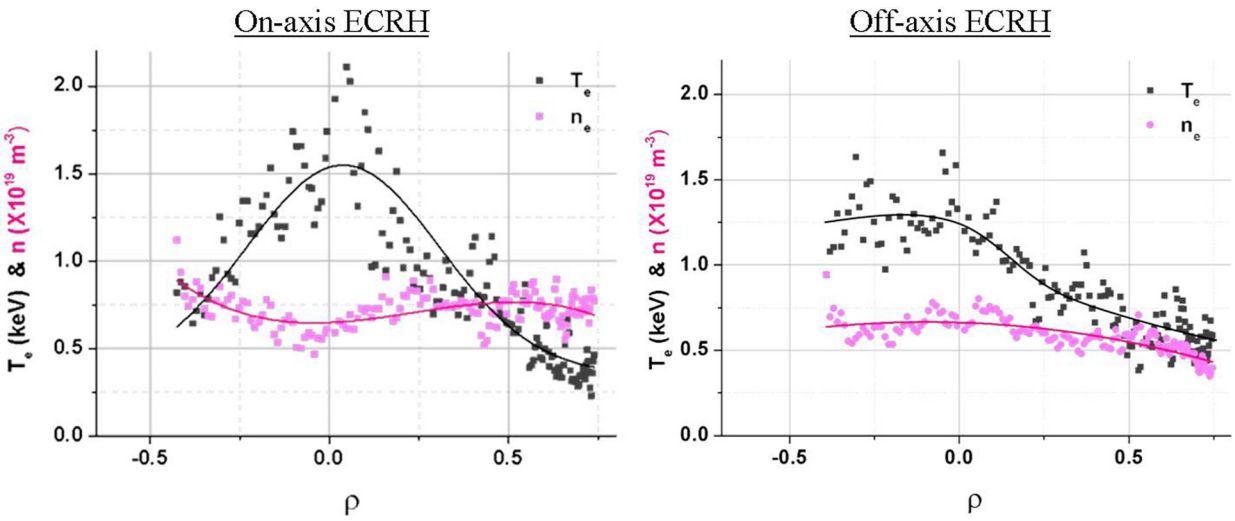

FIG. 2. (Left) On-axis ECRH electron temperature (black curve) and density profile (pink curve) for the normalized ρ value obtained by fitting the data from Thomson scattering profiles; (left) off-axis ECRH temperature (black curve) and density profiles (pink curve) as a function of normalized ρ value measured by Thomson scattering (where positive and negative ρ values correspond to low and high field sides, respectively).

shown in Figs. 3 and 4, respectively. Results are plotted over the contour plots of the vacuum magnetic flux surfaces in TJ-II.

In low density plasmas ($n_e \approx 0.4 \times 10^{19}$ m^{-3}), core plasma potential is positive with values less than 1000 V ($\pm$25 V), as presented in Fig. 3, which corresponds to a positive radial electric field (E_r) in agreement with neoclassical predictions.[26–28] It should be noted that the ambipolarity condition (i.e., the equality of ion and electron fluxes) has two stable roots in stellarators: the ion root with typically $E_r < 0$, usually achieved in high density plasmas, and the electron root with $E_r > 0$ that is typically realized when electrons are subject to strong ECRH heating, as in the plasma scenarios reported in the works.[26,29,30] The root mean square (RMS) of potential fluctuations increases radially inwards from values in the range of 15 V in the edge to 50 V in the plasma center.

Although the contour plots for potential and RMS of potential fluctuations seem rather close to the magnetic flux surfaces, some discrepancies should be noted. The 2D map for the absolute plasma potential (Fig. 3, left) has a local maximum that is slightly shifted (1–2 cm) upwards from the axis of vacuum magnetic flux surfaces to the high field side. The local maximum of RMS fluctuations of potential (Fig. 3, right) is also shifted upward. These shifts could be due to uncertainties in the beam trajectory calculations. The shift (in the range of 1 cm) is within the error bar for the calculation of the sample volume position. Moreover, the radial size of the SV is around 1–2 cm. In addition, top–bottom and LFS–HFS poloidal variation of average potential on vacuum magnetic surfaces is on the order of 50 V (Fig. 3). But it should be noted that this is comparable to the peak-to-peak level of experimental error for plasma potential achieved in the present

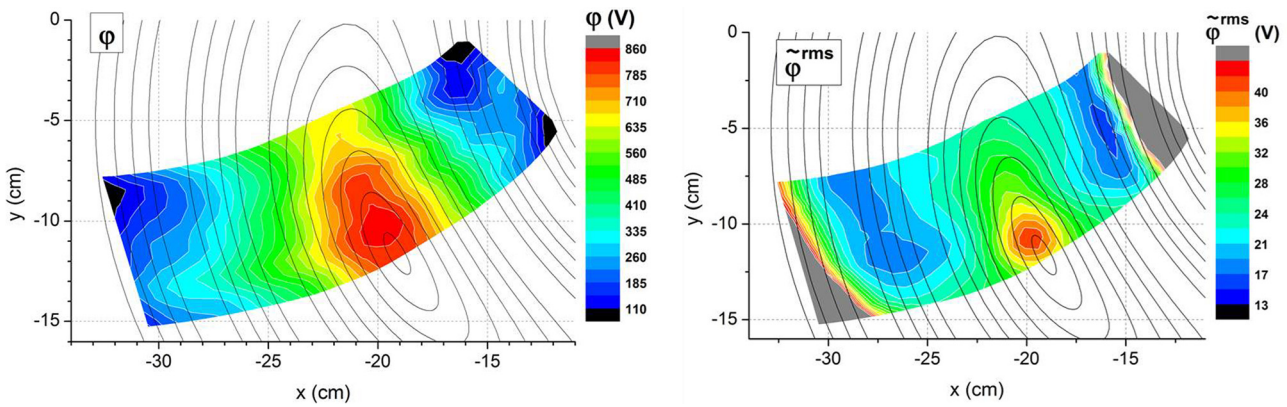

FIG. 3. 2D poloidal map of mean potential (left) and RMS potential fluctuations (right) for the line average densities ranging between 0.43 and 0.47 $\times$ 10^{19} m^{-3}; discharges presented (E_b changes from 128 keV to 148 keV, respectively): #44393, #44389, #44354, #44356, #44357, #44362, #44364, #44366, #44370, #44380, and #44388. Vacuum magnetic flux surfaces are shown in gray.

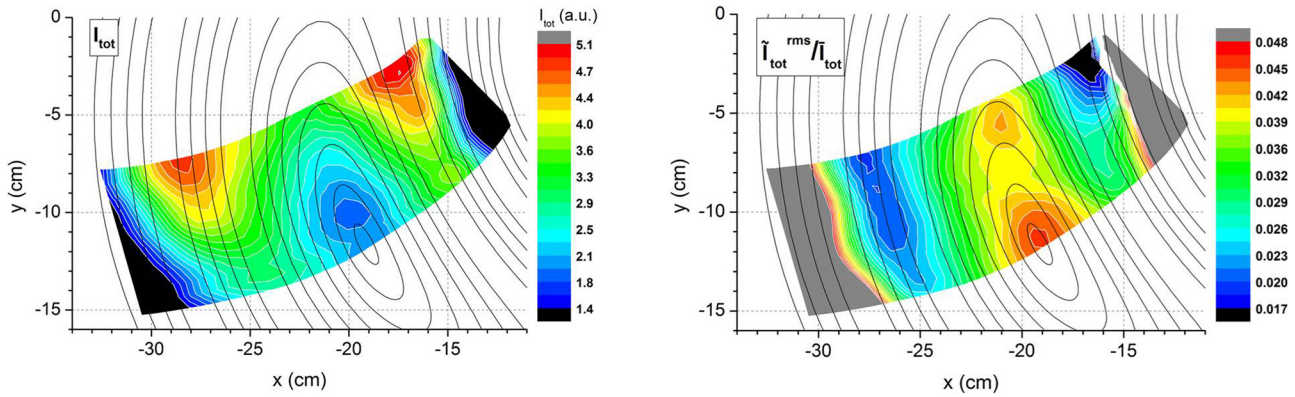

FIG. 4. 2D poloidal map for average (left) and normalized RMS (right) values of secondary ion current I_{tot}, which is a proxy of density fluctuations.

experiments. As shown in Fig. 3 right, in the explored plasma scenarios and within experimental uncertainties (±5 V) no evidence of strong spatial localization in RMS fluctuation levels in potential was observed.

The secondary ion current (I_{tot}) measured by the HIBP is proportional to the local plasma density for low-density plasmas, neglecting probing beam attenuation (see Sec. III B 3). Hence, a normalized level of secondary ion current fluctuations, $\tilde{I}_{tot}^{rms}/\bar{I}_{tot}$, is proportional to normalized density fluctuations $\tilde{n}/n$, and I_{tot} measurement is a proxy to the plasma density profile.

Figure 4 presents the 2D poloidal map for average (left) and normalized RMS (right) values of I_{tot}. A local minimum in the RMS of I_{tot} fluctuations is located at the position of the local maximum of the I_{tot} mean value (see Sec. III B). The up-down poloidal variation in total secondary current (Fig. 4, left) could be due to the variation of Cs^+ primary current with the E_b (in the range of 128–148 keV). The decrease in the Cs^+ ion energy also leads to the increase in primary trajectory length and causes attenuation of the probing beam. The uncertainty in the I_{tot} mean value (of the order of 20%) can be accounted for as being due to the variation of the discharges. In agreement with previous studies, edge and core fluctuations are dominated by frequencies below 100 kHz.[12,31]

B. Effect of ECRH on fluctuations

1. ECRH on-axis experiments

Figure 5 (left) presents the radial profiles of the normalized level of secondary ion current fluctuations for different primary beam energies for the results obtained during the 2D poloidal scan (see Fig. 4). A local minimum in the normalized fluctuation levels ($\tilde{I}_{tot}^{rms}/\bar{I}_{tot}$) appears both in the HFS and LFS at $\rho \sim 0.5$–0.6. This minimum appears for all beam energies (i.e., at different poloidal locations), illustrating the poloidal symmetry and reproducibility of experimental results. The radial location of these minima is correlated with the peaks (maximum) of the I_{tot} profile, i.e., the change from positive to negative radial gradients in I_{tot} profiles as

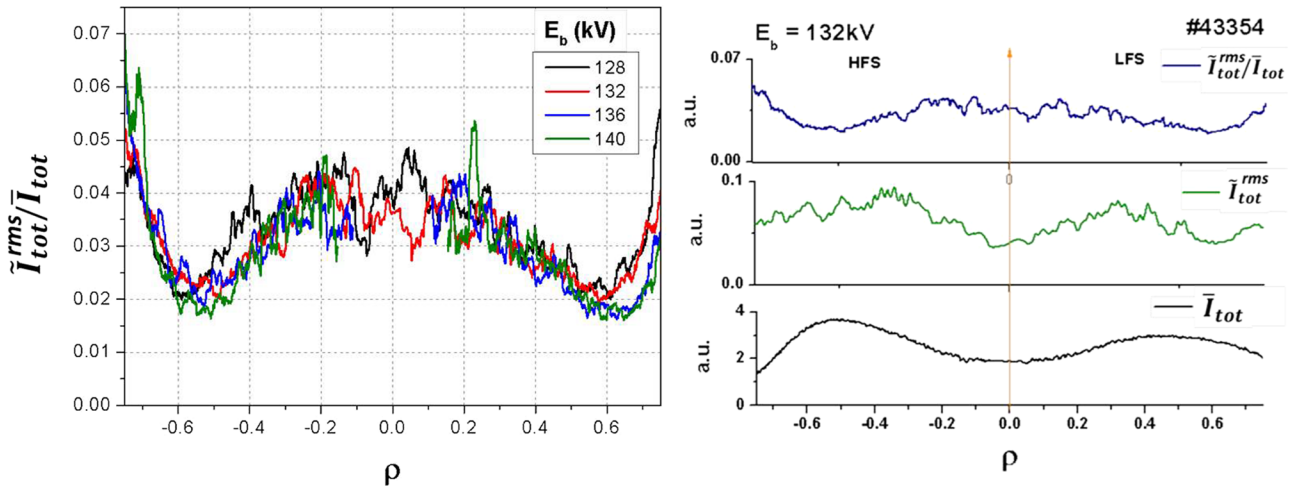

FIG. 5. Profiles of normalized RMS of the beam current fluctuation level for four beam energies (left); radial profiles for RMS fluctuation levels in I_{tot} and I_{tot} normalized ($\sim I_{tot}^{rms}/\bar{I}_{tot}$) values in the hollow density profile for on-axis ECRH plasma, $E_b = 132$ keV. The local minima are observed in I_{tot} relative fluctuations at the peaks of the I_{tot} profile (right).

shown in Fig. 5 (right). Figure 5 (right) also shows the relative RMS fluctuation in secondary ion current for a single scan ($E_b = 132$ keV) from the HFS to LFS along with the hollow secondary ion current profile in the low-density ECRH plasma.

The power spectrograms of density fluctuations along with the radial secondary ion current profile for on-axis ($\rho = 0$) ECRH plasma are plotted with respect to ρ in Fig. 6. The secondary ion current profile for on-axis ECRH indicates a more peaked shape and higher maximal value in the HFS at the border between negative and positive gradient regions ($\rho \approx -0.5$). The normalized level of density fluctuations ($\tilde{I}_{rms}/I$) is larger in the negative ($\rho = 0.7 - 1$) than in the positive ($\rho = 0.5 - 0.3$) density gradient region, with a minimum in the proximity of the zero density gradient region ($\rho \approx 0.6$). In the frequency range below 100 kHz, fluctuations are strongly dominated by quasi-coherent modes[32] that are localized in the positive density gradient region, ($|\rho| < 0.5$).

2. ECRH off-axis experiments

Figure 7 shows the mean secondary ion current, normalized level of density fluctuations, and power spectrogram of the secondary ion current measured by HIBP-II for off-axis ($\rho = 0.34$) ECR-heated plasmas. Power spectrograms for the two scans are presented with respect to the ρ value in Fig. 7. Fluctuations in the secondary ion current appear both in the positive and negative gradient regions, with the relative amplitude of density fluctuations higher in the negative I_{tot} gradient region (Fig. 7). Fluctuations are dominated by broadband frequencies (<100 kHz as shown in Fig. 7) in the negative I_{tot} density gradient region and eventually by quasi-coherent modes in the positive gradient region (off-axis ECRH scenarios). Furthermore, plasma density fluctuations are poloidally asymmetric, showing higher power and broader frequency spectra (f < 100 kHz) in the LFS than in the HFS (Fig. 7). Therefore, experimental results in off-axis ECRH scenarios show a clear influence of positive and negative I_{tot} gradient regions on plasma fluctuations with quasi-coherent modes located in the negative gradient region.

3. ECRH on-axis vs off-axis experiments

The power spectra of the normalized density fluctuations for on-axis and off-axis experiments are shown in Fig. 8. The level of fluctuations is larger in the negative ($\rho \approx 0.9 - 0.6$) than in the positive ($\rho \approx 0.5 - 0.2$) I_{tot} gradient in the whole frequency range (1–800 kHz) [Figs. 8(a) and 8(b)]. In the negative gradient region ($\rho \approx 0.6 - 0.9$), the amplitude of fluctuations above 100 kHz increases as core electron temperature increases (i.e., for on-axis ECRH). An opposite behavior is observed for frequencies below 100 kHz [Fig. 8(c)].

Finally, it should also be noted that secondary ion current profiles have a higher peaked amplitude at the transition from positive to negative gradient regions in LFS for off-axis ECRH plasma (see Fig. 7), unlike the on-axis ECRH profile (see Fig. 6). The origin of these differences in I_{tot} might be due to different beam trajectories and, as a result, different beam attenuations. As noted, the I_{tot} profile is a proxy but not the exact n_e profile. To get a proper n_e profile, even at low density, the inverse problem should be solved assuming the shape of beam trajectories, T_e profile, and beam injection current. The procedure to reconstruction plasma density profiles from HIBP secondary current measurements in TJ-II has been recently described.[33] In ECRH plasma scenarios, where beam attenuation effects are weak, the reconstructed density profiles are consistent with Thomson scattering data within experimental errors.[33] The profile of secondary ion current and its hollowness depends on beam attenuation, which depends both on plasma

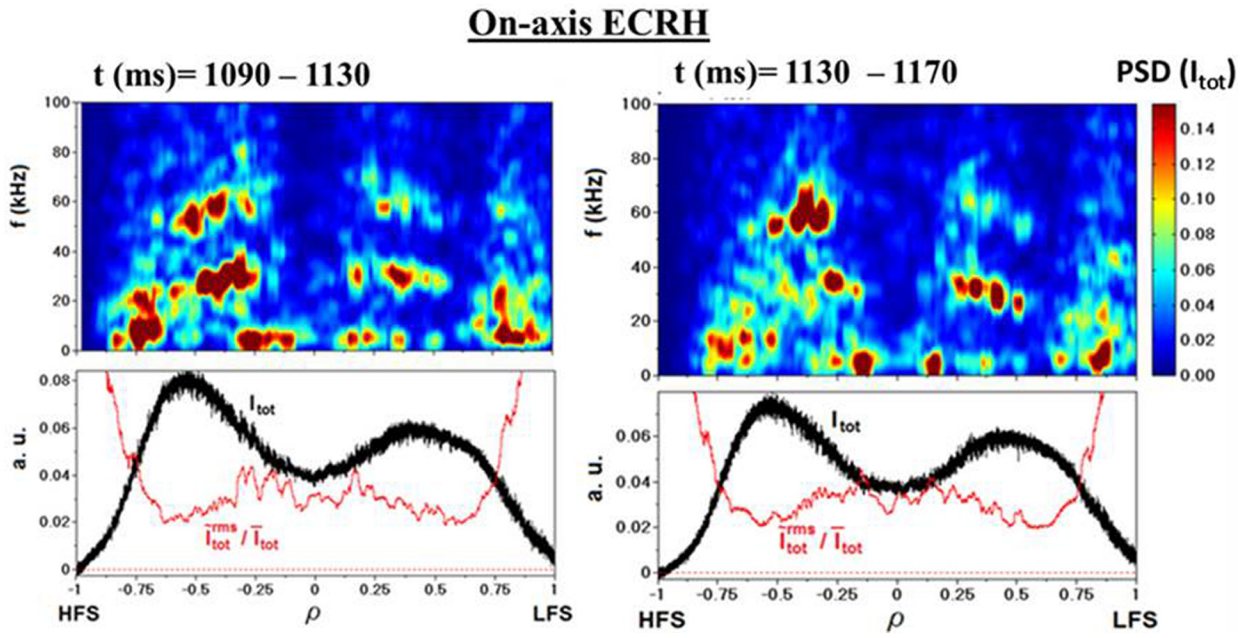

FIG. 6. On-axis ECRH plasma ($\rho = 0$). Power spectral density (PSD) of fluctuations in the secondary ion current with respect to ρ along with the secondary ion current profile (black curve) and the normalized RMS of its fluctuations (red curve), measured by HIBP-II plasma for two radial scans.

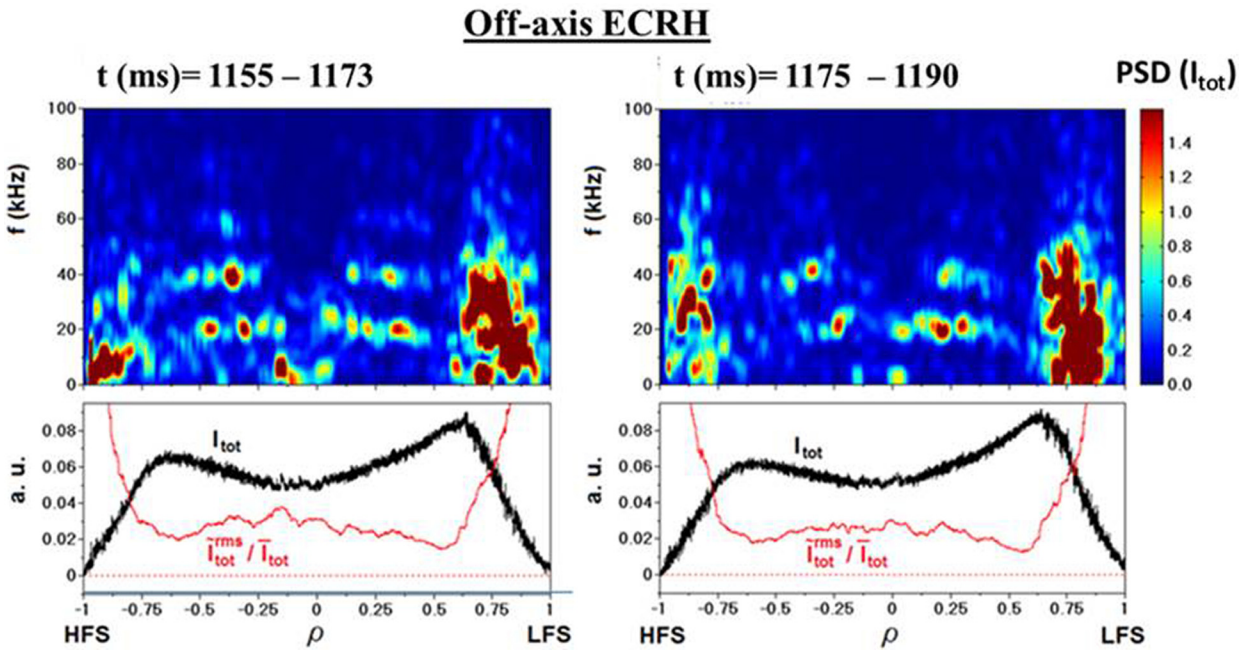

FIG. 7. Off-axis ECRH plasma ($\rho = 0.34$). Power spectral density of fluctuations in the secondary ion current with respect to ρ along with the secondary ion current profile (black curve) and the normalized RMS of its fluctuations (red curve), measured by HIBP-II for two radial scans.

electron density and electron temperature. In this particular case, the electron temperature is peaked (Fig. 2, left), so the effective ionization cross section is hollow, and the density profile is also hollow (also shown in Fig. 2, left), so these two factors lead to a more hollow I_{tot} profile. This effect is discussed in Ref. 33.

IV. CONCLUSIONS

Model validation requires the development of plasma diagnostics to show that a new model faithfully represents physics reality. From this perspective, the direct experimental characterization of plasma fluctuations in the whole plasma cross section is a great challenge for experimentalists and an important contribution for model validation of fluctuations in the regimes with positive and negative density gradient regions. HIBP was used in a wide energy scanning mode to successfully obtain 2D poloidal contour plots of plasma potential and density and their fluctuations have been measured in low density plasmas sustained by ECRH in the TJ-II stellarator. The new operational technique of the HIBP presented approximately one-third of the core plasma poloidal area to measure fundamental plasma parameters with the following conclusions:

(a) The 2D map for the absolute plasma potential has a local maximum in the plasma core as expected in low-density high-temperature scenarios. It shows about 1 cm mismatch with vacuum magnetic calculations that could be partially explained by instrumental effects. The 2D map for the absolute plasma potential shows poloidal symmetry within the experimental error ±25 V. The 2D map for the plasma potential RMS shows poloidal symmetry within ±5 V experimental uncertainty.

(b) Density fluctuations appear in both the positive and negative I_{tot} gradient regions for ECRH plasmas. Normalized density fluctuations are stronger in the negative I_{tot} density gradient than in the positive gradient region. Frequency spectra are dominated by frequencies below 100 kHz with different spectral characteristics in the positive and negative gradient regions that are affected by the ECRH scenario (on vs off-axis heating).

These observations are consistent with linear GK TEM simulation in ECRH plasma scenarios in the TJ-II stellarator where the most unstable modes appear in negative density and temperature gradient regions.[34] GK simulations of tokamaks have shown two types of density gradient driven modes:[19] a first mode is driven by a negative radial density gradient that corresponds to density gradient driven TEM instability and a second one driven by a positive radial density gradient. The TJ-II innovative experimental setup, developed using a dual HIBP diagnostic, paves the way to validate models on core plasma potential asymmetries and particle fueling under positive density gradient scenarios. On-going experiments are in progress to systematically quantify the influence of the shape of temperature and density profiles on the level of fluctuations and transport in the positive and negative gradient regions. Future work will include new experiments in order to expand the 2D mapping toward the whole TJ-II poloidal cross section.

Finally, it should be noted that 2D measurement of plasma potential, plasma density, and their fluctuations, together with the unique experimental arrangement of a dual plasma transport and

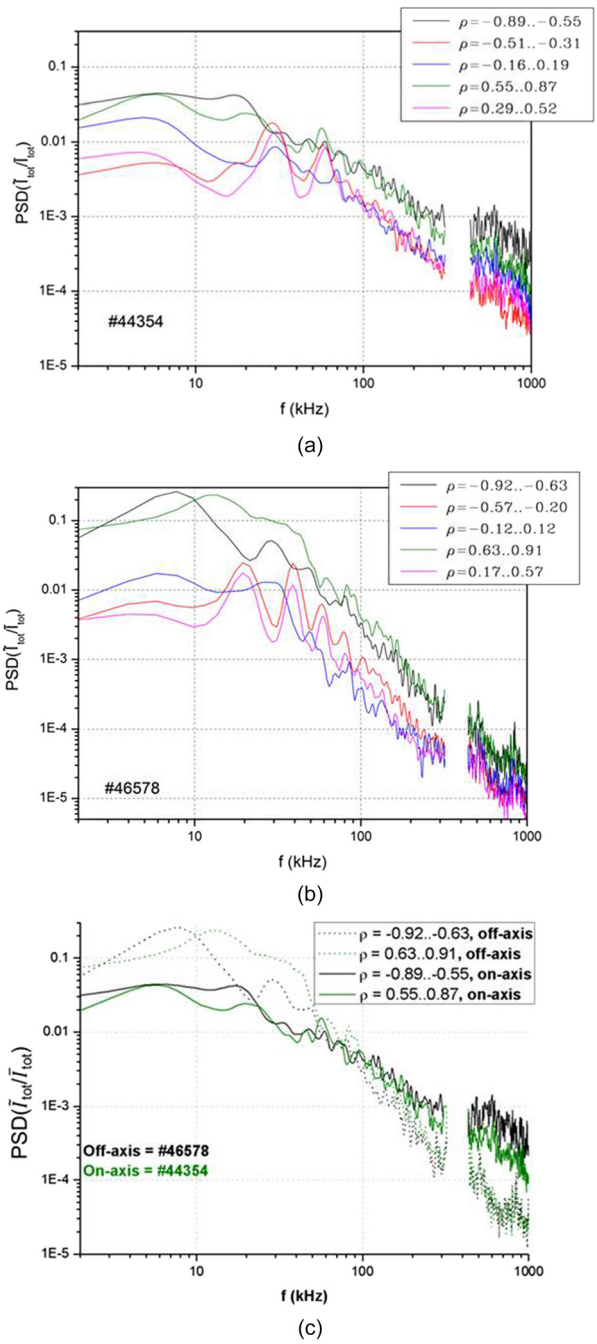

FIG. 8. Level of fluctuations for on-axis (a) and off-axis (b) ECRH plasma for different radial positions. (c) Over plotting off and on-axis fluctuations corresponding to the ρ value of the gradient region of density. The absence of data points around 400 kHz in (a)–(c) is due to instrumental effects.

turbulence[1] and the role of Alfvén eigenmodes in the development of zonal structure HIBP systems would provide key insights into interplay between[35] and the intertwining between turbulent and neoclassical mechanisms.[36]

ACKNOWLEDGMENTS

Research was sponsored in part by the Spanish regional research programme under Project No. Y2018/NMT-4750 (PROMETEO-CM). Research was sponsored in part by the Ministerio de Ciencia, Innovación y Universidades of Spain under Project No. PGC2018–097279-B-I00. The work of the Kurchatov team (Sec. III) was funded by Russian Science Foundation, Project No. 19–12-00312. The work of the Kharkiv team was funded by STCU Project P507. The work of A.V.M. was partly supported by the Competitiveness Program of NRNU MEPhI. IPFN activities received financial support from "Fundação para a Ciência e Tecnologia" through Project No. UID/FIS/50010/2019. This work has been carried out within the framework of the EUROfusion Grant Agreement No. 633053. The views and opinions expressed herein do not necessarily reflect those of the European Commission.

DATA AVAILABILITY

Raw data were generated at the TJ-II facility. Derived data supporting the findings of this study are available from the corresponding author upon reasonable request.

REFERENCES

[1]A. V. Melnikov, *2019 Electric Potential in Toroidal Plasmas* (Springer Nature Switzerland AG, 2019), p. 240.
[2]C. Hidalgo, Plasma Phys. Controlled Fusion **37**, A53 (1995).
[3]C. Hidalgo, J. Talmadge, M. Ramisch, and TJ-II, HXS, and TJ-K Teams, Plasma Phys. Controlled Fusion **59**, 014051 (2017).
[4]J. M. García-Regaña, C. D. Beidler, R. Kleiber, P. Helander, A. Mollén, J. A. Alonso, M. Landreman, H. Maaßberg, H. M. Smith, Y. Turkin *et al.*, Nucl. Fusion **57**, 056004 (2017).
[5]J. L. Velasco, I. Calvo, J. M. García-Regaña, F. I. Parra, S. Satake, J. A. Alonso, and LHD Team, Plasma Phys. Controlled Fusion **60**, 074004 (2018).
[6]I. Calvo, F. I. Parra, J. L. Velasco, J. Arturo Alonso, and J. M. García-Regaña, Nucl. Fusion **58**, 124005 (2018).
[7]T. Estrada, E. Sánchez, J. M. García-Regaña, J. A. Alonso, E. Ascasíbar, I. Calvo, A. Cappa, D. Carralero, C. Hidalgo, and M. Liniers, Nucl. Fusion **59**, 076021 (2019).
[8]M. A. Pedrosa, J. A. Alonso, J. M. García-Regaña, C. Hidalgo, J. L. Velasco, I. Calvo, R. Kleiber, C. Silva, and P. Helander, Nucl. Fusion **55**, 052001 (2015).
[9]P. Xanthopoulos, G. G. Plunk, A. Zocco, and P. Helander, Phys. Rev. X **6**, 021033 (2016).
[10]E. Sánchez, T. Estrada, J. L. Velasco, I. Calvo, A. Cappa, A. Alonso, and J. M. Garcia-Regana, in 27th IAEA Fusion Energy Conference (FEC), EX/P1-11 (2018).
[11]Z. Yan, G. R. McKee, R. Fonck, P. Gohil, R. J. Groebner, and T. H. Osborne, Phys. Rev. Lett. **112**, 125002 (2014).
[12]S. J. Zweben, J. A. Boedo, O. Grulke, C. Hidalgo, B. LaBombard, R. J. Maqueda, P. Scarin, and J. L. Terry, Plasma Phys. Controlled Fusion **49**, S1 (2007).
[13]A. Shimizu, T. Ido, M. Nishiura, S. Kato, K. Ogawa, H. Takahashi, H. Igami, Y. Yoshimura, S. Kubo, and T. Shimozuma, Rev. Sci. Instrum. **87**, 11E731 (2016).
[14]M. Valovic, K. Axon, L. Garzotti, S. Saarelma, A. Thyagaraja, R. Akers, C. Gurl, A. Kirk, B. Lloyd, G. P. Maddison *et al.*, Nucl. Fusion **48**, 075006 (2008).
[15]P. Vincenzi, F. Koechl, L. Garzotti, D. B. King, E. Tindale, T. Bolzonella, P. T. Lang, B. Pegourié, M. Romanelli, and R. Wenninger, Nucl. Fusion **55**, 113028 (2015).
[16]K. McCarthy, N. Panadero, S. K. Combs, N. Tamura, E. Ascasíbar, M. Calvo, A. Chmyga, T. Estrada, J. M. Fontdecaba, R. García *et al.*, Plasma Phys. Controlled Fusion **61**, 014013 (2019).
[17]A. Dinklage, R. Sakamoto, M. Yokoyama, K. Ida, J. Baldzuhn, C. D. Beidler, S. Cats, K. J. Mc Carthy, J. Geiger, M. Kobayashi *et al.*, Nucl. Fusion **57**, 066016 (2017).

[18]L. Garzotti, J. Figueiredo, C. M. Roach, M. Valovič, D. Dickinson, G. Naylor, M. Romanelli, R. Scannell, G. Szepesi *et al.*, Plasma Phys. Controlled Fusion **56**, 035004 (2014).
[19]C. Angioni, M. McDermott, E. Fable, R. Fischer, T. Pütterich, F. Ryter, G. Tardini, and ASDEX Upgrade Team, Nucl. Fusion **57**, 116053 (2017).
[20]D. Tegnered, M. Oberparleiter, H. Nordman, and P. Strand, J. Phys. **775**, 012014 (2016).
[21]F. Castejón, D. Alegre, A. Alonso, J. Alonso, E. Ascasíbar, A. Baciero, A. de Bustos, D. Baiao, J. M. Barcala, E. Blanco *et al.*, Nucl. Fusion **57**, 102022 (2017).
[22]I. S. Bondarenko, A. A. Chmuga, N. B. Dreval, S. M. Khrebtov, A. D. Komarov, A. S. Kozachok, and L. I. Krupnik, Rev. Sci. Instrum. **72**, 583 (2001).
[23]A. V. Melnikov, L. I. Krupnik, E. Ascasibar, A. Cappa, A. A. Chmyga, G. N. Deshko, M. A. Drabinskij, L. G. Eliseev, C. Hidalgo, P. O. Khabanov *et al.*, Plasma Phys. Controlled Fusion **60**, 084008 (2018).
[24]A. V. Melnikov, L. G. Eliseev, S. E. Lysenko, M. V. Ufimtsev, V. N. Zenin *et al.*, Nucl. Fusion **57**, 072004 (2017).
[25]A. V. Melnikov, L. G. Eliseev, R. Jiménez-Gómez, E. Ascasibar, C. Hidalgo, A. A. Chmyga, A. D. Komarov, A. S. Kozachok, I. A. Krasilnikov, S. M. Khrebtov *et al.*, Fusion Eng. Des. **96-97**, 724 (2015).
[26]A. V. Melnikov, K. S. Dyabilin, L. G. Eliseev, S. E. Lysenko, and Yu. N. Dnestrovskij, Probl. At. Sci. Technol. Ser. Thermonucl. Fusion. **54**, 54–73 (2011) (in Russian), available at http://vant.iterru.ru/vant_2011_3/4.pdf.
[27]J. L. Velasco, J. A. Alonso, I. Calvo, and J. Arevalo, Phys. Rev. Lett. **109**, 135003 (2012).
[28]C. Gutierrez-Tapia, J. J. Martinell, D. López-Bruna, A. V. Melnikov, L. Eliseev, C. Rodríguez, M. A. Ochando, F. Castejón, J. García, B. P. van Milligen *et al.*, Plasma Phys. Controlled Fusion **57**, 115004 (2015).
[29]A. V. Melnikov, C. Hidalgo, L. G. Eliseev, E. Ascasibar, A. A. Chmyga, K. S. Dyabilin, I. A. Krasilnikov, V. A. Krupin, L. I. Krupnik, S. M. Khrebtov *et al.*, Nucl. Fusion **51**, 083043 (2011).
[30]A. V. Melnikov, C. Hidalgo, T. Ido, A. Shimzu, A. Fujisawa, K. S. Dyabilin, and S. E. Lysenko, Plasma Fusion Res. **7**, 2402114 (2012).
[31]A. Ouroua, T. P. Crowley, K. A. Connor, D. R. Demers, A. Fujisawa, R. L. Hickok, P. E. McLaren, and P. M. Schoch, Fusion Eng. Des. **34-35**, 613 (1997).
[32]A. V. Melnikov, L. G. Eliseev, M. A. Ochando, K. Nagaoka, E. Ascasibar, A. Cappa, F. Castejon, T. Estrada, C. Hidalgo, S. E. Lysenko *et al.*, Plasma Fusion Res. **6**, 2402030 (2011).
[33]Ph. O. Khabanov, L. G. Eliseev, A. V. Melnikov, M. A. Drabinskiy, C. Hidalgo, N. K. Kharchev, A. A. Chmyga, A. S. Kozachek, I. Pastor, J. L. de Pablos *et al.*, J. Instrum. **14**, C09033 (2019).
[34]E. Sánchez, T. Estrada, J. L. Velasco, I. Calvo, A. Cappa, A. Alonso, and J. M. García-Regaña, Nucl. Fusion **59**, 076029 (2019).
[35]Z. Qiu, L. Chen, F. Zonca, and W. Chen, Nucl. Fusion **59**, 066031 (2019).
[36]R. Gerrú, S. Mulas, U. Losada, F. Castejón, B. Liu, T. Estrada, B. Ph. van Milligen, and C. Hidalgo, Nucl. Fusion **59**, 106054 (2019).